Photon echo, spectral hole burning, and optically detected magnetic resonance in ^{171}Yb^{3+}:LiNbO$_3$ bulk crystal and waveguides

Federico Chiossi [●],[1,*,†] Eloïse Lafitte-Houssat,[1,2,*] Kangwei Xia,[3] Fiammetta Sardi [●],[3] Zhonghan Zhang,[1,4]
Sacha Welinski [●],[2] Perrine Berger,[2] Loic Morvan,[2] Varvara Foteinou,[5] Alban Ferrier,[1,6] Diana Serrano,[1] Roman Kolesov,[3]
Jörg Wrachtrup,[3] and Philippe Goldner[1,‡]

[1]*Chimie ParisTech, PSL University, CNRS, Institut de Recherche de Chimie, Paris, 75005, France*
[2]*Thales Research and Technology, Palaiseau, 91767, France*
[3]*3. Physikalisches Institut, University of Stuttgart, 70569 Stuttgart, Germany*
[4]*Shanghai Institute of Ceramics, Chinese Academy of Sciences, Heshuo Road 585, Jiading, Shanghai, 201899, China*
[5]*RUBION, Ruhr University Bochum, Bochum, 44780, Germany*
[6]*Faculté des Sciences et Ingénierie, Sorbonne Université, Paris, 75005, France*

Recent progress in the realization of high-quality optical resonators and waveguides along with the possibility to incorporate rare-earth ions, make lithium niobate a promising material to build integrated platforms for quantum information processing. ^{171}Yb^{3+} is a particularly attractive system because it can show long coherence lifetimes at zero magnetic field thanks to transitions insensitive to magnetic field fluctuations. In this paper, we investigate the optical and spin properties of ^{171}Yb^{3+} ions in LiNbO$_3$ bulk crystals as well as implanted waveguides. Using hole-burning spectroscopy and optically detected magnetic resonance, we studied ground and excited state hyperfine structures and probed optical and spin spectral holes. Importantly, the hole linewidths suggest that part of the ions in the waveguides are in a similar environment as in the bulk sample. We furthermore characterized spin population relaxation and coherence lifetimes of ^{171}Yb^{3+} ions in the bulk crystal at temperatures between 50 mK and 9 K. At low temperatures, T_2 up to 9.5 μs (34 kHz homogeneous linewidth) and spin relaxation rates as long as $\approx$100 ms were measured. Our results show that ^{171}Yb^{3+}:LiNbO$_3$ is a system that exhibits narrow optical homogeneous linewidths over a 50 GHz bandwidth together with an electron spin degree of freedom. This is of interest for a variety of applications in integrated quantum photonics such as quantum memories or quantum processors.

I. INTRODUCTION

Rare-earth (RE) ions in crystals have been recently pointed out as promising platforms for optical quantum technology [1,2], as their long optical and spin coherence lifetimes (T_2) stand out among solid-state systems [3]. They are actively considered for building quantum memories for light [4], microwave (MW) to optical quantum transducers [5], or quantum processors [6]. For RE Kramers ions like Nd^{3+}, Er^{3+} or Yb^{3+}, magnetic fluctuations originating from the RE themselves or the crystal host are often the main dephasing process because of their large electronic magnetic moments [7]. Indeed, very long optical and hyperfine coherence lifetime of 4.4 ms and 1.3 s, respectively, have been achieved in Er^{3+}:Y$_2$SiO$_5$ (YSO) by suppressing RE electron spin flips with a large external magnetic field and low temperatures, whereas the YSO matrix shows low nuclear magnetic moments [8,9].

Alternatively, an enhancement of the coherence lifetime can be obtained in ions for which conditions to reach so-called zero first-order Zeeman (ZEFOZ) transitions have been established. This is because the frequency of such transitions is insensitive to magnetic field perturbations at first order [10]. By applying 1.3 T along a well-defined direction and dynamical decoupling pulses, a ZEFOZ ground-state hyperfine transition with the exceptional coherence lifetime of 6 h has been found for non-Kramers ^{151}Eu^{3+} ions (nuclear spin $I = 5/2$) in YSO [11]. Similar effects have been observed for Pr^{3+} ($I = 5/2$) in YSO [12] and La$_2$(WO$_4$)$_3$ [13]. Although finding ZEFOZ transitions usually requires a precise knowledge of the Hamiltonian of the system and are obtained for very specific conditions, nonzero nuclear spin isotopes of Kramers RE ions, in sufficiently low site symmetries, are naturally provided with ZEFOZ optical and spin transitions at zero magnetic field [14]. This is due to a symmetric mixing of electron and nuclear spin wave functions through the hyperfine interaction which causes all level energies to be independent of small magnetic fields at first order. Thus, optical and spin T_2 in the ms range have been observed in ^{171}Yb^{3+} ($I = 1/2$, electron spin $S = 1/2$) doped YSO, exceptionally long values for a Kramers RE ion at zero magnetic field [14–16]. The same effect led to a 28-fold enhancement

---

*These authors contributed equally to the work.
†federico.chiossi@chimieparistech.psl.eu
‡philippe.goldner@chimieparistech.psl.eu

for ground-state hyperfine coherence lifetimes in ^{167}Er:YSO ($I = 7/2$, $S = 1/2$) crystals [17]. The strong potential of the hybridized electron-nuclear hyperfine levels of the ^{171}Yb^{3+} isotope for optical quantum technologies has been recently highlighted in YSO and YVO$_4$ crystals. For instance, they are promising for the realization of efficient MW to optical transducers [18,19], optical storage with long memory time and large bandwidth [16], as well as quantum processors and single photon sources [20]. In particular, the possibility to operate at zero magnetic field is attractive for interfacing these materials with superconducting qubits to create networks of quantum processing nodes.

Integration into photonic circuits combining waveguides, micronano resonators, and electrodes is also highly desirable for compact multifunctional designs showing enhanced interaction with light and, e.g., MW fields [20–25]. In this regard, lithium niobate, LiNbO$_3$ (LN), a well-known material for its large electro-optical coefficient and nonlinearity, has become one of the most widely used on-chip platforms [26], with many applications including coherent photon conversion [27], fast electro-optic modulators [28], and quantum technologies [29]. Incorporating RE ions in LN waveguides or resonators can provide additional functionalities for the latter field, and several works have been already devoted to this subject [30–34], building on studies on bulk RE-doped LN crystals [35,36]. In particular, Yb:LN single ion detection was recently reported in an implanted lithium niobate on insulator (LNOI) thin film [25]. Spectral hole burning (SHB) in bulk Yb:LN crystals has also been studied at temperatures down to 9 K [37]. The properties of the ^{171}Yb^{3+} isotope were, however, not assessed in these previous works.

Here we study an isotopically enriched ^{171}Yb^{3+} doped LN bulk crystal of congruent composition at temperatures between 50 mK and 9 K. In particular, we report on optical coherence, spectral diffusion, as well as hyperfine structures and spectral hole lifetimes, properties that are key to the development of ^{171}Yb:LN integrated quantum photonic platforms. In this regard, the spin and spectral hole linewidths, along with the optically detected magnetic resonance (ODMR) spectra, are compared to those obtained in a LNOI thin film waveguide in which the ^{171}Yb^{3+} doping has been achieved by implantation.

The paper is organized as follows: After a brief introduction on the crystal structure and description of our experimental setups, we present the results in six subsections. We explore the optical absorption and emission spectra in Sec. IV A. In Secs. IV B–IV D, we discuss ODMR, hole burning spectra under magnetic field, and ground-state spin relaxation. Two- and three-pulse photon echo measurements are presented in Secs. IV E and IV F.

II. CRYSTAL STRUCTURE AND Yb^{3+} MAGNETIC PROPERTIES

LN crystal structure belongs to the R3c space group (No. 161) and has no inversion center. Both Li$^+$ and Nb^{5+} sites have a C$_3$ axial symmetry with the rotation axis parallel to c, and thus the substituting trivalent RE ions should possess the same C$_3$ site symmetry. However, the presence of vacancies and charge compensating defects may reduce the local

symmetry to C$_1$, as proven in different RE-doped LN crystals through electron paramagnetic resonance (EPR) and optical spectroscopy. In addition, several nonequivalent sites have been identified by EPR in nearly stoichiometric crystals, while the very broad lines in congruent crystals prevent detailed analysis [35,38–41].

The ^{171}Yb^{3+} isotope has the simplest hyperfine structure owing to both the electron and nuclear spins being equal to 1/2. The four hyperfine levels of every crystal field level can be approximated by the following Hamiltonian:

$$\mathbf{H} = \mu_B \mathbf{B} \cdot \mathbf{g} \cdot \mathbf{S} + \mathbf{I} \cdot \mathbf{A} \cdot \mathbf{S} - \mu_n g_n \mathbf{B} \cdot \mathbf{I}, \qquad (1)$$

where μ_B and μ_n are the Bohr and nuclear magnetons and $g_n = 0.9885$ [42]. The three terms represent the electronic Zeeman interaction, the hyperfine coupling, and the nuclear Zeeman interaction with $\mathbf{S}$ and $\mathbf{I}$ the electronic and nuclear spin operators, $\mathbf{A}$ and $\mathbf{g}$ the hyperfine and electronic Zeeman tensors, and $\mathbf{B}$ the magnetic field.

The C$_3$ site symmetry implies that the $\mathbf{A}$ and $\mathbf{g}$ tensors have one principal direction along the c axis and two equivalent ones perpendicular to c. At zero external magnetic field, the hyperfine structure is thus composed of two singlets and one doublet. On the contrary, there is no condition on the tensors in the C$_1$ site symmetry and the level degeneracy is completely removed [14].

The analysis of the EPR lines in a stoichiometric Yb:LN crystal reveals nine different Yb^{3+} centers, six of which have C$_1$ site symmetry and slightly different ground-state $\mathbf{g}$ tensors [41]. In all cases, their off-diagonal entries are small (<0.5) and the diagonal g values quite close to those of Yb^{3+} in the three different C$_3$ sites, namely, $g_\parallel = 4.46$ and $g_\perp = 2.70$. The presence of defects thus results in a weak perturbation of the C$_3$ symmetry, with a small tilt of the $\mathbf{g}$ tensor orientation away from the axial principal axes. Regarding the hyperfine parameters, only the C$_3$ sites have been taken into account with $A_\parallel = 3.57$ GHz and $A_\perp = 2.14$ GHz for the ^{171}Yb^{3+} isotope in one site and $A_\parallel = 4.50$ GHz and $A_\perp = 2.25$ GHz in another one. For congruent crystals, like the sample in this paper, a prevalence of quasi-C$_3$ centers can be reasonably assumed.

III. EXPERIMENTAL METHODS

A congruent LN crystal with [Li]/([Li]+[Nb]) = 48.5% and doped with 50 ppm (nominal concentration) of isotopically enriched ^{171}Yb^{3+} (95%) was grown using the Czochralski method. The sample was then oriented using a Laue diffractometer and cut so the light could propagate on a length of 12.5 mm with a polarization either parallel or perpendicular to the crystalline c axis. ^{171}Yb^{3+} ions were also incorporated in z-cut (surface perpendicular to c) LNOI thin films (NANOLN, China) by implantation technique. The implantation was performed at the RUBION institute of the Ruhr University Bochum employing an ion energy of 1.5 MeV and a fluence of 10^{12} ions/cm^2. The estimated doping concentration is 3 ppm. The sample was postannealed at 700 °C for 8 h. To increase the excitation volume, the ^{171}Yb:LNOI thin film was further shaped into 8-mm-long straight waveguides spaced by 30 μm by means of electron beam lithography
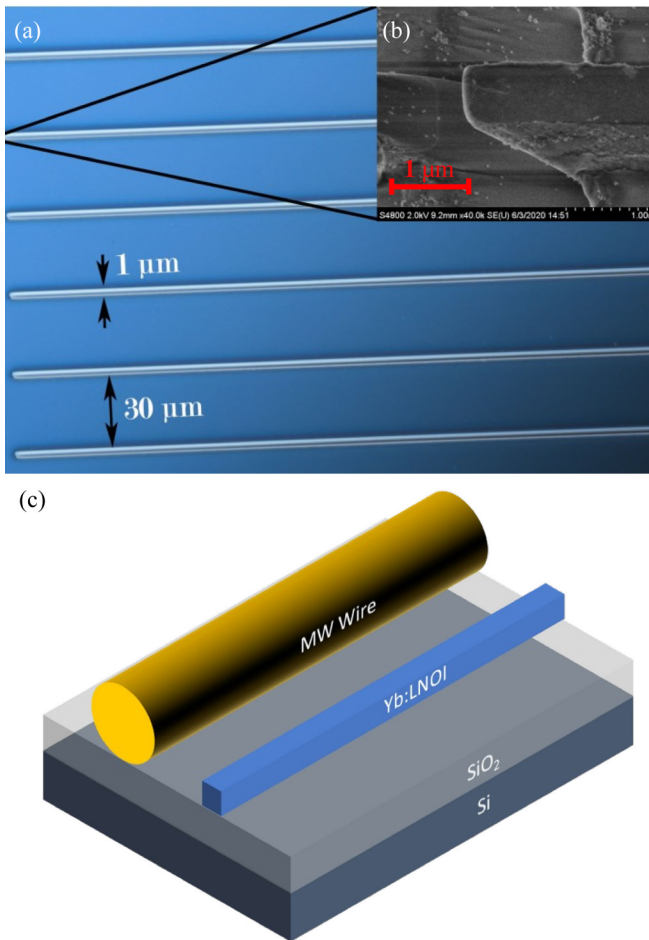
FIG. 1. (a) Optical microscope image of LNOI waveguides. (b) Scanning electron microscope image of the 45° undercut used to redirect light out of the sample plane. (c) A microwave wire was stretched parallel to the waveguide to resonantly drive ^{171}Yb^{3+} spins.

and reactive ion etching [see Fig. 1(a)]. Further details on the waveguides can be found in Ref. [25].

Spectroscopic experiments were carried out using three different setups. The emission spectrum of the bulk crystal was recorded through a spectrometer (Princeton Instruments Acton SP2300) coupled to a ICCD camera (Princeton Instruments Pi-MAX 4) after the sample was excited by an optical parametric oscillator pumped by a Nd:YAG laser (Ekspla NT342B-SH) with a 6-ns pulse duration and 5 cm^{-1} full width at half maximum (FWHM) linewidth. The emission decay was recorded using a photomultiplier tube (ET Entreprises 9658B). The crystal temperature was maintained at 11 K by a CTI-Cryogenics cryocooler. The measurements using this setup are presented in Sec. IV A.

The ODMR, as well as the MW and optical hole burning spectra of the ^{171}Yb:LNOI waveguide and, for comparison, of the ^{171}Yb:LN bulk crystal, were obtained with a second setup. These results are reported in Sec. IV B and at the end of Sec. IV C. The setup is composed by a homemade single mode diode laser tuned externally around 980 nm and by a home-built confocal microscope constructed on the basis of a custom built continuous flow cryostat (CryoVac) equipped with a vacuum-compatible nanopositioning stage

(nPoint, travel range 100 μm × 100 μm × 25 μm). The laser is capable of delivering up to 1 mW of power to the cryostat. The sample was mounted on a cold finger (5 K) placed on a 3D stepper motor with a 10 mm travel range in all three directions for coarse positioning of the sample. A microscope objective lens (Zeiss, Epiplan-Neofluar, 0.95NA 100x Vak) was used to focus the excitation laser onto the end of the waveguide and to collect the resulting fluorescence. The end of the waveguide was undercut at 45° to redirect the fluorescence from in-plane waveguide toward the objective lens [see Fig. 1(b)]. Optical spectral holes were measured tuning the diode laser in resonance with ^{171}Yb^{3+} at a wavelength of ~980.5 nm (vacuum) and by splitting the laser beam in two beams that went through acousto-optic modulators (AOM) in double-pass configuration to serve as pump and probe. The probe beam frequency was swept around the pump one, which was kept fixed.

Spin transitions were investigated with the same setup by ODMR. A copper wire of 20 μm in diameter was placed parallel to the waveguide ~40 μm away from it [see Fig. 1(c)]. It was contacted to the outside of the cryostat with coaxial cables using a vacuum feedthrough equipped with SubMiniature version A (SMA) connector. The output connector was terminated with 50 Ω to minimize MW reflections. Two MW sources (SMIQ 03b, Rhode & Schwarz and HMC-T2220, Analog Devices) were combined using a home-made MW resistive splitter/combiner and sent into the cryostat through a MW amplifier (ZHL-42, Mini-Circuits). For the experiments with the bulk ^{171}Yb:LN sample, a similar MW wire was stretched on its surface. Laser-excited ^{171}Yb^{3+} fluorescence detected from the confocal volume 30–40 μm away from the wire and several microns below the sample surface was then monitored while the MW source frequency was swept. An increment of the fluorescence intensity with wavelength >1 μm, detected by a superconducting single photon detector (Scontel), revealed a spin transition at the current MW frequency. While for the ODMR experiment we used only one MW source being swept over a wide range, for the spin-hole measurements one of the MW sources had a fixed frequency in resonance with one of the spin transitions while the other one was swept in the vicinity of the probed spin resonance. The fluorescence was finally recorded as a function of the MW frequency.

High-resolution absorption and hole-burning spectra as well as photon echoes were recorded in the ^{171}Yb:LN bulk crystal on a third setup (Secs. IV A, C, D–F). Here the crystal was mounted in a closed cycle dilution refrigerator (Bluefors SD) and cooled at temperatures between 50 mK and 9 K. Temperatures were measured on the mixing chamber base plate. At the lowest temperatures, the repetition rate of the laser pulses was reduced so as to limit the average heating power on the crystal to the μW range. A helium bath cryostat (Janis SVT-200) equipped with homemade Helmholtz coils was used for SHB under magnetic field. A tunable diode-laser (Toptica DL Pro) with a linewidth of ~1 MHz FWHM was used as the excitation source. Laser frequency was measured by a wave meter (Burleigh WA-1100) with a resolution of 100 MHz while frequency sweeps were calibrated with a Fabry-Pérot interferometer (Toptica, 1 GHz free spectral range). A 80-MHz AOM (AA Opto-Electronics) driven by an
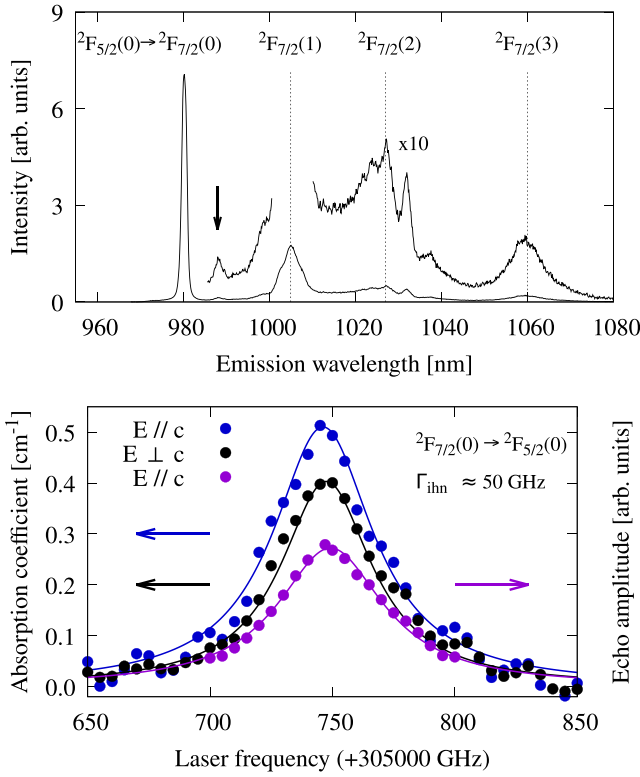
FIG. 2. Top: Emission spectrum recorded at 11 K exciting the 50 ppm ^{171}Yb:LN bulk crystal at 957 nm. Transitions are labeled according to Ref. [51]. The peak indicated by the arrow is believed to originate from the coupling with a localized phonon mode. Bottom, blue and black circles, left scale: Polarized absorption spectra at 10 K. Center frequency corresponds to 980.5 nm (vacuum). Bottom, purple circles, right scale: Photon echo amplitude as a function of the laser frequency at 1 K. The delay between the excitation and rephasing pulses was fixed at 5 μs. Lines represent Lorentzian fits.

arbitrary waveform generator (Agilent N8242A) was used to create pulses for the SHB and photon echo experiments. For the latter, square pulses with a 1.5 μs length and $\sim$10 mW power were typically used. Spectral holes were burned using 500-ms-long pulses of about 10 mW power and then probed with a much reduced power of about 100 μW. The laser beam went through a half-wave plate to set the light polarization parallel or perpendicular to the c axis and was focused on the sample by a 300 mm lens. Light was finally detected by a photodiode (Thorlabs PDB150A) connected to a digital oscilloscope (LeCroy WR6200).

IV. RESULTS

A. Absorption and emission properties

The unpolarized emission spectrum of the 50 ppm ^{171}Yb:LN sample at 11 K (Fig. 2, top) and the measured lifetime of the $^2F_{5/2}(0)$ level, $T_1 = 440 \mu$s, are similar to those reported previously at higher concentrations [37]. The absorption spectra for the $^2F_{7/2}(0) \rightarrow {}^2F_{5/2}(0)$ transition for light polarizations parallel and perpendicular to c are displayed in Fig. 2, bottom. The spectra show broad Lorentzian shapes that can be attributed to the high concentration of point defects in

TABLE I. Main spectroscopic parameters of rare-earth transitions in different matrices at liquid helium temperatures and zero magnetic field.

	f [10^{-6}]	λ^a [nm]	Γ_{ihn} [GHz]	Γ_h [kHz]
Yb:LN 50 ppm[b,c]	0.55	980.52	50	35
Yb:Y$_3$Al$_5$O$_{12}$ 500 ppm [45]	1.1	968.57	3.6	
Yb:YSO 10 ppm[b,d] [15]	0.38	978.85	0.55	1.1
Yb:YVO$_4$ 100 ppm[b] [18]	15.8	984.5	0.28	
Er:LN 80 ppm [35]	1.4	1532.06	180	>700
Tm:LN 0.1% [39]	4.0	794.22	90	28
Pr:LN 0.1% [1,46]	0.08	617	1700	76

[a]In vacuum, 0-0 transition.
[b]^{171}Yb^{3+} isotope enrichment.
[c]This paper.
[d]Site 2.

the form of vacancies and antisites in the congruent crystal [43,44]. The hyperfine transitions cannot be resolved due to an inhomogeneous linewidth of $\approx$50 GHz FWHM, in agreement with the values estimated in natural abundance Yb^{3+}:LN [37], but narrower than the linewidths found for other RE ions in LN (see Table I).

As the induced electric dipole contributes most to the transition [47], we can calculate the transition oscillator strength from the integrated absorption as [48]

$$f = 4\pi\epsilon_0 \frac{m_e c}{\pi e^2} \frac{1}{N} \frac{9n}{(n^2+2)^2} \int \alpha(\nu)d\nu, \qquad (2)$$

where ϵ_0 is the vacuum permittivity, e, m_e the electron charge and mass, c the speed of light, N the Yb^{3+} ions density, taken as the nominal one, $\alpha(\nu)$ the absorption coefficient at frequency ν, and n the refractive index. At 980.5 nm and cryogenic temperatures, the refractive index values perpendicular and parallel to the c axis are $n_\perp = 2.23$ and $n_\parallel = 2.18$ [49]. We thus obtain $f_\parallel = 5.5 \times 10^{-7}$ and $f_\perp = 4.0 \times 10^{-7}$ that are compatible with the line strength determined in Ref. [47] but smaller than the oscillator strength of Yb^{3+} in other matrices or other RE transitions of interest in lithium niobate (see Table I).

The spontaneous emission rate on the $^2F_{5/2}(0) \rightarrow {}^2F_{7/2}(0)$ transition can be calculated as follows :

$$A_{0\rightarrow 0} = \frac{2\pi e^2 \nu^2}{\epsilon_0 m c^3} \frac{1}{3} \frac{n(n^2+2)^2}{9}(f_\parallel + 2f_\perp) = 361 \text{ s}^{-1}.$$

Assuming a unit emission quantum yield, we estimate an emission branching ratio of $\beta = T_1 A_{0\rightarrow 0} \approx 16\%$. Given the high-quality fabrication techniques available in LN, this value makes Yb:LN a promising system to reach high Purcell factors in optical cavities [25,50].

B. Optically detected magnetic resonance

Spin transitions in a ^{171}Yb:LN bulk crystal and a ^{171}Yb:LNOI waveguide were determined by ODMR at 5 K, as described in Sec. II. Figures 3(a) and 3(b) show the ODMR spectra which reveal three peaks located at 0.7, 2.0, and 2.9 GHz in good agreement with the ground state A parameters previously determined by EPR [41]. The linewidths, on
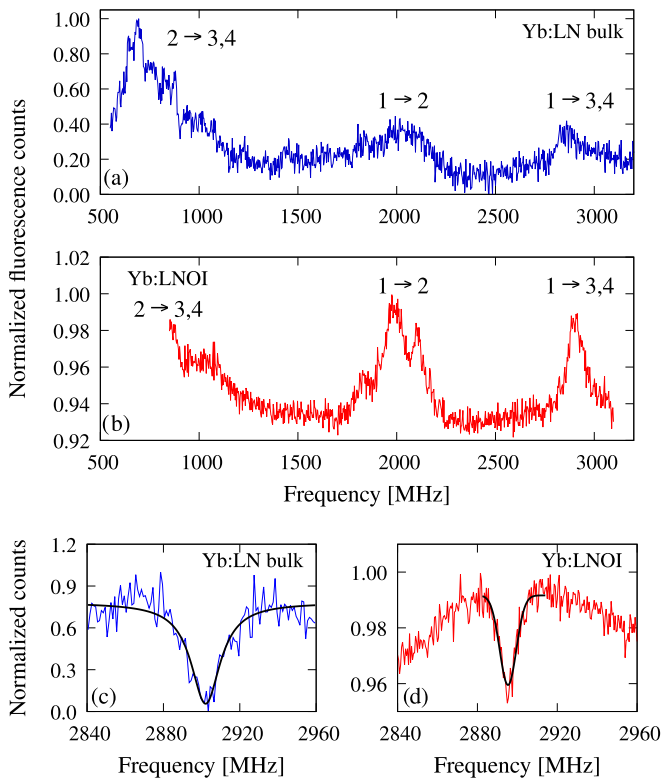
FIG. 3. (a), (b) ODMR spectra of ^{171}Yb:LN bulk crystal and ^{171}Yb:LNOI waveguide. The labels refer to the energy levels in Fig. 4 (right). (c), (d) MW spectral holes burnt at 2900 MHz in the $1 \rightarrow 3, 4$ spin transition in ^{171}Yb:LN bulk crystal and ^{171}Yb:LNOI waveguide. Linewidths are respectively 19 and 10 MHz FWHM. Black lines represent Lorentzian fits. All experiments were performed at 5 K.

the order of 100 MHz FWHM, are not unexpected in congruent LN due to the large defect concentration. Presence of different Yb^{3+} sites is further illustrated by the three peaks composing the transition at 2.0 GHz in Fig. 3(b) or the broad feature at ∼0.7 GHz in Fig. 3(a). Nonetheless, the ground-state hyperfine structure seems to be consistent with a C_3 site

symmetry as a single transition peak is found at 2.9 GHz. The corresponding hyperfine structure is shown in Fig. 4, right. It is worth noting that the ODMR contrast in the ^{171}Yb:LNOI waveguide appears to be enhanced with respect to the bulk crystal. It could be due to the LNOI film having the c axis perpendicular to its surface while the bulk LN crystal had the c axis in plane. This might have led to different polarization selection rules for both optical and MW transitions. This, in turn, might explain the differences in ODMR contrast.

To further analyze the spin transition linewidth, we performed SHB experiments in the MW domain. In the experiment, a MW pump excitation was set at the peak of the 2.9 GHz transition, while a MW probe was swept around the pump frequency. As shown in Figs. 3(c) and 3(d), both the bulk crystal and the waveguide show a dip, with a linewidth of 19 and 10 MHz FWHM, respectively, when the pump and probe frequencies match. These values give upper limits (9.5 and 5 MHz, respectively) on the spin effective homogeneous linewidths at long times, i.e., including spectral diffusion. They are also likely to contain contribution from power broadening given the large values observed compared to those measured on optical spectral holes (see Sec. IV C). The broader hole observed in the bulk crystal could be related to its higher doping concentration and/or higher content in paramagnetic impurities or defects.

C. Optical spectral hole burning

Hole-burning spectra were recorded at 1 K by tuning the laser to the center of the $^2F_{7/2}(0) \rightarrow {}^2F_{5/2}(0)$ transition and setting a 5 ms delay between burn and probe pulses to allow for complete relaxation of the excited state. Measurements were repeated for magnetic fields B from 0 to 20.1 mT with steps of 2.9 mT along or perpendicular to the c axis and for different laser polarizations. Some spectra are displayed in Fig. 4. At zero field, broad holes are detected at relative frequencies of ± 3.9, 3.4, 2.9, and 0.6 GHz. Few shallow antiholes are also recognized, for instance, at 2.1 GHz. The transmission peak in the range (5.5–6.0) GHz which becomes clearer with the increase in magnetic field is believed to
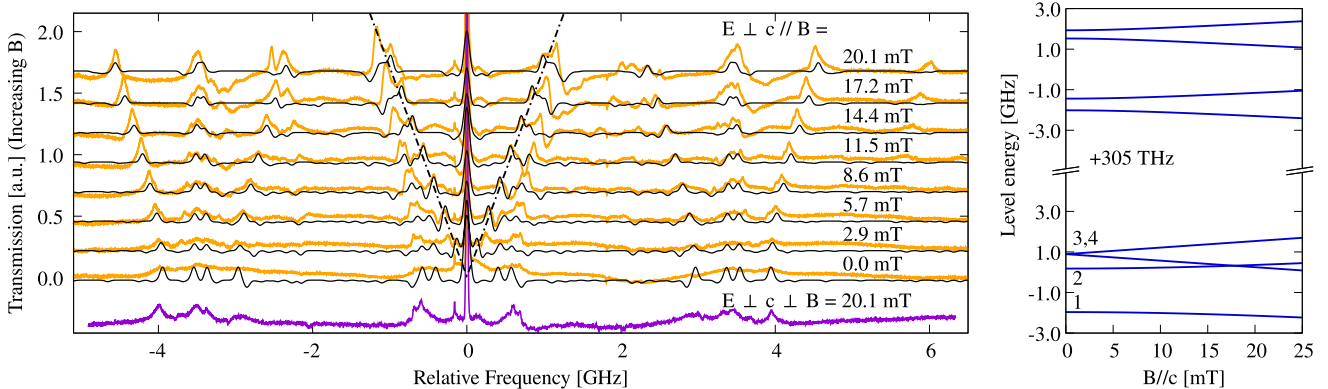

FIG. 4. Left: Experimental (orange) and simulated (black) optical SHB spectra for different external magnetic fields oriented along the c axis. In purple, the spectrum acquired with the maximum magnetic field (20.1 mT) directed perpendicular to the c axis. A vertical shift has been added for clarity. The dotted lines highlight the linearly shifting holes attributed to $^{171}Yb^{3+}$ ions in C_3 sites or impurities of even Yb^{3+} isotopes. The narrow peak at -160 MHz is an artifact caused by an AOM. Experiments were performed at 1 K. Right: Simulated $^2F_{7/2}(0)$ and $^2F_{5/2}(0)$ hyperfine level energies as a function of magnetic field along the c axis.

TABLE II. Hyperfine parameters (GHz) and *g* factors of ^{171}Yb^{3+} ground and excited states in LN.

	$A_{\perp,1}$	$A_{\perp,2}$	$A_{\parallel}$	$g_{\parallel}$	$g_{\perp}$
^{2}F$_{7/2}$(0) [41]	2.14	2.14	3.57	4.5	2.7
^{2}F$_{5/2}$(0) (this paper)	0.98	0.17	6.93	3.5	

be an antihole that appears as a hole because of fast spin relaxation [52]. Broad holes with a complex structure, like those at around ±3.4 GHz, are consistent with the results of the ODMR experiments (Sec. IV B) and the congruent composition of the crystal [1,41].

By inspecting the SHB spectra acquired for different magnetic fields applied along *c*, we can identify two symmetric holes that arise from the central hole and shift linearly (dotted lines in Fig. 4). Fitting their relative frequencies as a function of the field strength, we infer $g_{\parallel} = 3.52 \pm 0.03$. All the other holes seem to be due to singlet levels. Their frequency is insensitive to small magnetic fields, proving that the corresponding transitions are ZEFOZ in nature. As a consequence, the degeneracy of ^{2}F$_{5/2}$(0) seems to be already completely lifted at zero magnetic field which is compatible with a C$_1$ site symmetry but not with a C$_3$ one. This lowering of symmetry was not observed for the ground-state hyperfine structure in the ODMR experiments (see Sec. IV B), which could be explained by crystal-field perturbations having different effects on ground and excited electronic wave functions.

The only two linearly shifting side holes thus probably originate from a few C$_3$ centers or, more likely, from even Yb^{3+} isotope impurities which represent a few percent of the total Yb^{3+} amount.

Taking into account the number of parameters required to fully describe ^{171}Yb^{3+} ions in a C$_1$ site, the need to include different sites, and the broad experimental features, a comprehensive understanding of the hole-burning spectra is difficult to achieve. Nonetheless, we provide in the following a simple model to roughly predict the hyperfine structure at any arbitrary magnetic field. We consider only one center and assume a weakly perturbed C$_3$ symmetry that can be described by the C$_3$ diagonal **g** and **A** tensors but with two distinct values $A_{\perp,1}$, $A_{\perp,2}$. For the ground state, we use **A** and **g** determined for the C$_3$ symmetry in Ref. [41]. Note that the parameters of the two ground-state tensors **g** and **A** should not affect the holes positions in the spectrum but only those of the antiholes. As g$_{\parallel}$ has already been determined, the three diagonal entries $A_{\parallel}$, $A_{\perp,1}$, $A_{\perp,2}$ of the excited state **A** tensor are the only free parameters that need to be adjusted to the experimental hole positions with *B* ∥ *c*, according to Eq. (1).

The *A* parameters found by fitting the calculated holes positions to the experimental ones for the eight *B* values are summarized in Table II and the simulated spectra, including holes and antiholes, are drawn in black in Fig. 4 (left), assuming equal branching ratios for all transitions. The hole/antihole amplitude ratio was set to 3:−1, and the linewidths to 80 MHz FWHM, similar to the widths seen in ODMR (Sec. IV B). Holes and antiholes of even Yb^{3+} isotopes impurities have been added to the simulated spectra for completeness. The hyperfine level energy dependence on
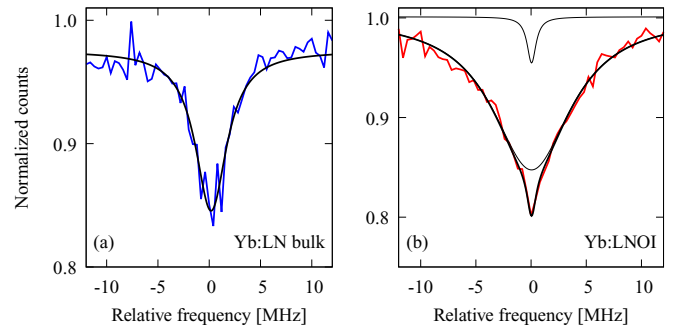

FIG. 5. (a), (b) Optical spectral holes burnt in ^{171}Yb:LN bulk crystal and ^{171}Yb:LNOI waveguide. Linewidths (FWHM) determined by Lorentzian fits (black lines) are 3 MHz (a), and 1 and 9 MHz (b). Experiments were performed at 5 K.

the magnetic field along *c* is also displayed in Fig. 4. In this scheme, only transitions from the two lower ground-state levels have a ZEFOZ nature.

By applying magnetic fields perpendicular to *c*, no shifts in hole frequencies were observed, as shown by spectra obtained without magnetic field (lowest orange trace in Fig. 4) and with the highest field (violet trace). In particular, no linearly shifting holes were observed, indicating a small value of the $g_{\perp}$ factor. This agrees with the expected ratio $A_{\parallel}/A_{\perp} = g_{\parallel}/g_{\perp}$ that predicts $g_{\perp} < 0.5$.

Spectral hole linewidths (FWHM) were also compared between the ^{171}Yb:LN bulk crystal and ^{171}Yb:LNOI waveguide at 5 K and zero magnetic field (see Sec. II). The experimental results are plotted in Fig. 5. According to a fitting procedure based on Lorentzian shapes, the width of the central hole in the bulk ^{171}Yb:LN is 3 MHz. The hole in the implanted ^{171}Yb:LNOI waveguide shows two components with widths of 1 and 9 MHz, respectively. The broader component in the waveguide compared to the bulk sample could be due to the damages in the crystal structure induced by the implantation process and not completely cured by the annealing treatment. The narrower component has however a width smaller than the bulk value, showing that part of the ions are in an environment with a low defect density.

In a previous study [25], the hole width in a natural abundance Yb^{3+} implanted LNOI waveguide was found to be 80 MHz, one order of magnitude larger than what we observe with ^{171}Yb^{3+}. It indicates the magnetic origin of the main fluctuations that perturb Yb^{3+} transition frequency in LN and the effectiveness of the ZEFOZ transition of ^{171}Yb^{3+} in reducing the effect of these fluctuations.

D. Spin population relaxation

The decay of the hole amplitude as a function of the delay between burn and probe pulses shows how the nonequilibrium distribution of the three hyperfine level populations induced by the laser excitation relaxes through different spin-flip processes. To estimate their rates and temperature dependence, we measured the hole depth in the ^{171}Yb:LN bulk crystal between 5 ms and 700 ms after the burn pulse and at different temperatures. An example of the hole depth decay at 1 K is shown in the inset of Fig. 6. All decays were well fitted by the
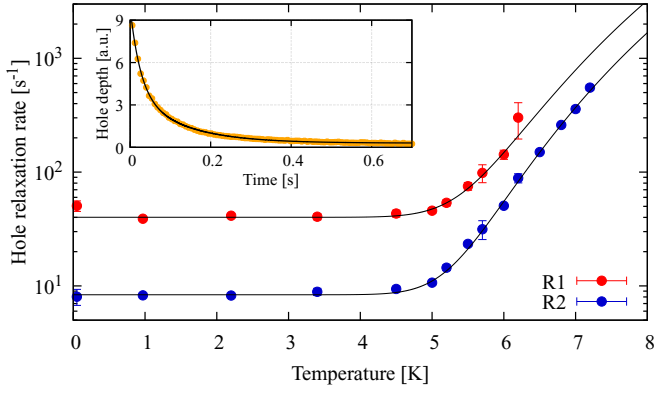
FIG. 6. Inset: Optical hole depth as a function of delay after burning ($T = 1$ K). (Main) Temperature dependence of the two hole relaxation rates (circles) and fit using Eq. (4) (lines).

function

$$h(x) = c_1 e^{-R_1 t} + c_2 e^{-R_2 t} + c_3. \tag{3}$$

The offset c_3 may represent levels with very slow relaxation rates, like the minutes-long spectral hole reported in Er:LN caused by the superhyperfine interaction with ^{7}Li (92% abundance, $I = 3/2$) and ^{93}Nb (100% abundance, $I = 9/2$) [39]. Equation (3) has been used to estimate the two relaxation rates R_1 and R_2 for temperatures up to 6.2 K. As shown in Fig. 6, above 5 K the two rates increase exponentially with the temperature T so starting from 6.2 K only the slowest component R_2 can be accurately assessed. Both rates follow the equation

$$R_{1,2}(T) = R_{1,2}^0 + \frac{a}{e^{\Delta E^s / k_B T} - 1}, \tag{4}$$

where k_B and a are the Boltzmann and coupling constants. The fitting procedure gives $R_1^0 = 40.1 \pm 0.8\,\mathrm{s}^{-1}$, $R_2^0 = 8.4 \pm 0.2\,\mathrm{s}^{-1}$, $\Delta E_1^s = 56.4 \pm 5.6\,\mathrm{cm}^{-1}$, and $\Delta E_2^s = 59.6 \pm 1.2\,\mathrm{cm}^{-1}$. The first term in Eq. (4) is temperature independent and attributed to flip-flop processes between ground-state spin levels. The second one corresponds to a coupling with phonon modes. Note that the activation energies $\Delta E_{1,2}^s$ for the two rates are close to each other but much lower than the crystal field level energy expected in an Orbach process [53]. This point is discussed in the next section as this phenomenon also appears in the temperature dependence of the optical homogeneous linewidth.

E. Two-pulse photon echo

The optical homogeneous linewidth (Γ_h) and the mechanism responsible for its broadening were assessed by performing photon echo measurements between 50 mK and 9 K, at zero magnetic field.

In the inset of Fig. 7, the peak intensity of the two-pulse photon echo as a function of the delay time τ_d between the excitation and rephasing pulses is shown for three temperatures. In the first microseconds, the intensity decay follows a pure exponential function $I(\tau_d) \propto \exp(-4\tau_d / T_2)$ where T_2 is the coherence lifetime, indicating that spectral diffusion does not affect the transition homogeneous linewidth in this time interval. However, it could play a role at longer delays
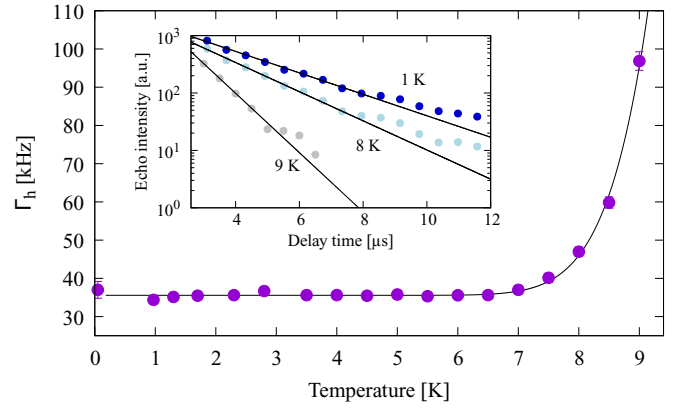

FIG. 7. Inset: Two-pulse photon echo decay at three different temperatures. Exponential fits are shown as black lines. Main: Homogeneous linewidth, obtained through two-pulse photonecho measurements, as a function of temperature (circles) and fit using Eq. (5) (black line).

causing the observed deviation from the exponential fit. In fact, in the case of a dephasing process due to spin flips near a ^{171}Yb^{3+} ion, frequency shifts can be reversed by another flip of the same spins, thereby partially reviving the initial ^{171}Yb^{3+} ion coherence [39,54]. Alternatively, such a deviation may originate from subensembles of ions in environments with lower defect concentration and therefore endowed with longer coherence lifetimes.

The temperature dependence of the homogeneous linewidth, calculated from the coherence lifetime as $\Gamma_h = 1/\pi T_2$, is displayed in the main panel of Fig. 7. Remarkably, a 35 kHz optical homogeneous linewidth is observed below 6 K. This value is much closer to those measured for the non-Kramers Tm^{3+} ions in LN ($\Gamma_h = 30$ kHz) [39] rather than for the Kramers Er^{3+} ions ($\Gamma_h > 700$ kHz). The latter attain such narrow linewidths only when an external magnetic field is applied [35]. As already mentioned for spectral hole widths in Sec. IV C, low Γ_h values are attributed to ^{171}Yb^{3+} ZEFOZ transitions, which efficiently reduce the effect of magnetic noise. The larger effective homogeneous linewidth deduced from hole widths, about 1.5 MHz, is attributed to additional processes like slow spectral diffusion, laser drifts, or power broadening.

As in the case of hole relaxation, the homogeneous linewidth increases with increasing temperature and is well described by the expression

$$\Gamma_h(T) = \Gamma_0 + \frac{\Gamma_{\mathrm{ph}}}{e^{\Delta E / k_B T} - 1}, \tag{5}$$

where the plateau up to 7 K is represented by the term Γ_0 and the exponential increase above 7 K is due to the coupling with phonons in the ground and excited states. The best-fit results are $\Gamma_0 = 35.5 \pm 0.2$ kHz, $\Delta E = 87.3 \pm 3.2\,\mathrm{cm}^{-1}$, and $\Gamma_{\mathrm{ph}} = 69 \pm 36$ GHz for the phonon coupling coefficient. The same exponential energy factor ΔE has been reported for the homogeneous linewidth temperature dependence in the range from 12 to 19 K by fitting spectral hole profiles in Yb^{3+} doped congruent LN [37]. However, as already observed in other crystals [45], this value does not agree with Yb^{3+} energy

levels as ~ 250 cm^{-1} separate $^2F_{7/2}(0)$ and $^2F_{5/2}(0)$ from the next crystal field levels [51]. Interestingly, a peak at a similar ΔE energy (~ 85 cm^{-1}) with respect to the $^2F_{5/2}(0) \rightarrow ^2F_{7/2}(0)$ energy appears in both the absorption [51] and emission spectra of Yb:LN (Fig. 2). This peak could be due to the coupling between Yb^{3+} and a localized phonon mode, which would explain the temperature dependence of the optical dephasing. A similar mechanism, but with a smaller activation energy, could be responsible for the temperature dependence of the ground state spin lifetime (Sec. IV D).

The nearly constant coherence lifetime below 6 K indicates that interactions with two-level systems (TLSs) do not significantly contribute to the homogeneous linewidth. According to the standard TLS model [55], Γ_h should scale with T^α with $\alpha \sim 1.3$ while a plateau is found. Moreover, it should be stressed that the TLS contribution is not even quantifiable in ^{171}Yb^{3+}:LN whereas it has been identified as the main dephasing factor for Pr^{3+} in LN [46]. This discrepancy may be attributed to a larger structural disorder in this sample which presents a huge inhomogeneous linewidth compared to Yb:LN (see Table I).

As shown in many studies on RE-doped crystals [2], magnetic fluctuations are likely to dominate dephasing in ^{171}Yb:LN at low temperature. They can be caused by the nuclear spin bath of ^{7}Li, ^{93}Nb and ^{6}Li (8% abundance, $I = 1$), ^{171}Yb^{3+} ions themselves, and other paramagnetic impurities or defects. We first examine the nuclear spin contribution, noting that it is consistent with the constant coherence lifetime below 6 K as no nuclear spin polarization is expected even at 50 mK.

We estimated the nuclear spin contribution by considering a simple model where homogeneous linewidths are given by [10,14]

$$\Gamma_h = S_1 \delta B + S_2 \delta B^2, \tag{6}$$

where δB is the magnetic noise produced by flipping electron and nuclear spins in the crystal and $S_1 = 0$ for the ZEFOZ levels. This model assumes fast spin bath dynamics, in agreement with the observed quasiexponential photon echo decays.

For the main site identified in the SHB study (Sec. IV C), $g_\perp$ is found much smaller than $g_\parallel$ in the excited state. As a result, the second-order perturbation on the energy of a given ZEFOZ excited state level by δB is mainly due to the parallel component $\delta B_\parallel$. It is given by $\pm(\mu_B g_\parallel \delta B_\parallel)^2 / 4\Delta E$ where ΔE is the (positive) zero field energy difference to the closest hyperfine level (see Appendix). This gives a mean second-order sensitivity for the excited levels of $S_2 = 1.2 \times 10^3$ GHz/T^2. The same calculation can be carried out for the ZEFOZ levels of the ground state, taking into account in this case $\delta B_\perp$, as detailed in the Appendix. The average sensitivity of the ZEFOZ optical transitions is then estimated as $S_{2,\text{opt}} \approx 600$ GHz/T^2.

The magnetic noise δB due to LN nuclear spins can be estimated from the optical homogeneous linewidths of about 700 kHz measured at low magnetic field in Er^{3+} [35]. With a S_1 coefficient for the optical transition of 1-2 μ_B [56], this gives $\delta_B = 25 - 50$ μT. Another estimation can be obtained considering that $\delta B \propto \sum g_{n,i} n_i$ [57], where the sum is performed over the different nuclear spin species. The ratio of magnetic noise between LN and YSO is thus found to be 11,

leading to $\delta B \approx 33$ μT since the magnetic noise in YSO is about 3 μT [14]. Using Eq. (6), such a noise gives a second-order contribution to Γ_h of only 500 Hz. Even taking account bias magnetic field up to 50 μT, i.e., the earth magnetic field, the nuclear spin bath dephasing amounts to about 4 kHz, whereas we measure an homogeneous linewidth of 35 kHz.

This estimation must, however, be considered as a lower limit. This simple approach cannot capture the full dynamics of ^{171}Yb^{3+} ions interacting with the nuclear spin bath and does not take into account effects like the detuning of nearby nuclear spins by electron spins. This so-called frozen core effect, which decreases magnetic noise for Er^{3+} [35], should be much lower for ^{171}Yb^{3+} since the superhyperfine interaction vanishes to first order for the ZEFOZ levels. Nevertheless, it suggests that noise generated by ^{171}Yb^{3+} ions themselves, and possibly other paramagnetic defects, have a significant contribution to the measured optical homogeneous linewidth.

In the case of dephasing produced by the ^{171}Yb^{3+} spin bath, it should be noted that the ground-state hyperfine structure shown in Fig. 4 leads to a strong spin polarization (85%) in the lowest level at 50 mK. This should strongly reduce the associated magnetic noise but no increase of the coherence lifetime was measured. This could be explained by a negative $A_\parallel$ parameter that would reverse the spin energy level order. In this case, polarization in the three lowest levels would occur, which does not prevent spin flips and therefore magnetic noise. This partial polarization could also explain the nearly constant hole decay rates between 1 and 0.05 K. Indeed, a strong polarization to a single level should significantly change the decay rates. The ^{171}Yb^{3+} spin bath fluctuations should also be fast enough, on the order of 10s of μs, to lead to the nearly exponential photon echo decays shown in Fig. 7. Such fast rates would not be observed in spectral hole decays, where they would be hidden by the optical excited state decay ($T_1 = 440$ μs). In 10 ppm ^{171}Yb:YSO, flip-flop rates of about 500 s^{-1} have been observed [15], and it is conceivable that higher values could be reached in our 50 ppm ^{171}Yb:LN samples. In any case, additional experiments using high-quality samples with lower ^{171}Yb^{3+} concentration are needed to clarify dephasing processes and coherence lifetime upper limit.

Finally, we registered the echo amplitude for a fixed delay as a function of the laser frequency while maintaining the same excitation intensity. The values follow a Lorentzian distribution with a linewidth of ≈ 50 GHz FWHM, similar to the absorption inhomogeneous broadening (Fig. 2). When the absorption coefficient is small, the echo amplitude is indeed proportional to the number of excited ions, and therefore to the absorption coefficient. In terms of frequency multiplexing, ^{171}Yb:LN thus offers a large operational bandwidth giving up to $\Gamma_{\text{Inh}}/\Gamma_h = 10^6$ addressable channels or qubits.

F. Three-pulse photon echo

We further investigated spectral diffusion in ^{171}Yb:LN by performing three-pulse photon echo experiments at 1 K. The delay time τ_d is defined as the time interval between the first two pulses and T_w as the waiting time between the second and third pulses. The peak intensity of the stimulated photon echo, which appears after a delay τ_d from the third pulse, is
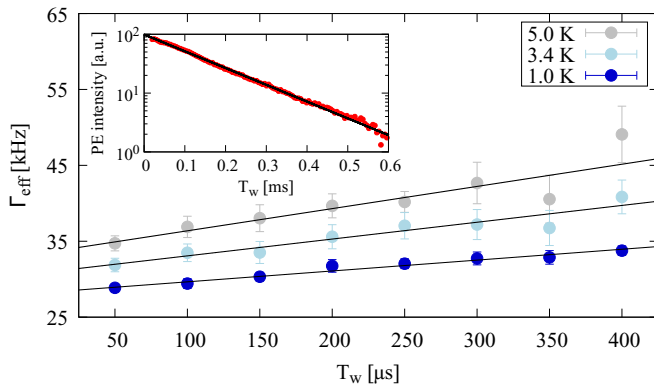
FIG. 8. Three-pulse photon echo experiments. Main: Effective homogeneous linewidth estimated from Eq. (7) versus waiting time at three temperatures. The black lines are linear fits. Inset: Photon echo peak intensity as a function of waiting time for $\tau_d = 2.5\,\mu$s and at $T = 1$ K. The black line is a fit using Eq. (7).

determined by a time-dependent effective linewidth $\Gamma_{\text{eff}}(\tau_d, T_W)$ and expressed as [7]

$$I(\tau_d, T_w) = I_0 e^{-2T_w/T_1} e^{-4\tau_d \pi \Gamma_{\text{eff}}}. \tag{7}$$

For fixed values of T_w, we measured the photon echo intensity as a function of τ_d and extracted Γ_{eff} by a pure exponential fitting. The obtained Γ_{eff} is linearly proportional to T_w as shown for three temperatures in Fig. 8. Spectral diffusion is attributed to interactions with the spin bath and the effective homogeneous linewidth is thus expected to depend on the waiting time according to [7]

$$\Gamma_{\text{eff}} = \Gamma_0 + 0.5\Gamma_{\text{SD}}[R\tau_d + 1 - \exp(-RT_w)]. \tag{8}$$

Here, Γ_{SD} and R are the maximum broadening caused by the spin dynamics and the characteristic spin-flip rate. Since Γ_{eff} was found to depend linearly on T_w, we conclude that $R\tau_d \ll RT_w \ll 1$ in the probed time interval (50–400 μs) so $\Gamma_{\text{eff}} \approx \Gamma_0 + 0.5\Gamma_{\text{SD}}RT_w$. The intercepts of the linear functions are indeed close to the homogeneous linewidth deduced from two-pulse photon echoes. Spectral diffusion up to a timescale of 400 μs is moderate, with $0.5\Gamma_{\text{SD}}R$ slopes varying from 14 kHz/ms to 30 kHz/ms in the 1–5 K range.

Finally, we studied the three-pulse photon echo intensity at 1 K as a function of T_w with $\tau_d = 2.5\,\mu$s (Fig. 8). The experimental data were fitted with Eq. (7), using the previous result to take into account the dependence of Γ_{eff} on T_w. We obtained $T_1 = 327 \pm 4\,\mu$s, similar to the $^2F_{5/2}$ lifetime of 440 μs measured by fluorescence decay.

V. CONCLUSION

A detailed study of the optical and spin properties of ^{171}Yb^{3+} ($I = 1/2$, $S = 1/2$) in lithium niobate, one of the most promising materials for integrated optical quantum technologies, has been performed. Optical SHB experiments under magnetic field, as well as ODMR spectroscopy, were used to determine hyperfine structures and spin Hamiltonian parameters in bulk samples as well as in implanted waveguides fabricated in LNOI thin films. First, optical ZEFOZ transitions, insensitive to magnetic field to first order, were

clearly identified at zero magnetic field in the hole burning spectra. Second, it was found that the excited state structure can be described with a perturbed C_3 symmetry model, whereas the ground-state one is consistent with a regular C_3 symmetry. Linewidths of spectral holes burned in optical and spin transitions were probed and showed that much narrower lines are obtained with ^{171}Yb^{3+} compared to samples doped with natural abundance Yb^{3+} thanks to the zero-field ZEFOZ transitions. Moreover, comparison of hole width between bulk and implanted waveguide samples suggests that some ions sit in similar environments in both materials. Spin relaxation times were measured through spectral hole decay and can reach between 25 and 100 ms in the bulk crystal at low temperature, limited by ground-state flip-flops.

In bulk samples, two-pulse photon echo amplitude was measured as a function of optical frequency and followed the 50 GHz broad inhomogeneous absorption profile. This technique was used to determine homogeneous linewidths and a value of 35 kHz was found below 6 K and under zero magnetic field, similar to values obtained for non-Kramers ions in LN, highlighting again the ZEFOZ effect. At higher temperatures, the increase in homogeneous linewidth is attributed to coupling with localized phonon modes. A simple model suggests that nuclear spins do not limit coherence lifetimes and that samples with lower dopant or paramagnetic defect concentrations could show longer T_2. Spectral diffusion was finally studied by three-pulse photon echoes and found on the order of 10s of kHz/ms.

These results show that ^{171}Yb^{3+}:LN is a promising system for obtaining emitters with narrow optical linewidth and an electron spin degree of freedom in high-quality photonic structures. This could be exploited to build broadband integrated quantum memories for light, single ion-based quantum processors or lifetime-limited single photon emitters.

APPENDIX

The effects of magnetic field fluctuations are estimated for ^{171}Yb^{3+} starting from the hyperfine interaction that gives zero field splittings and ZEFOZ levels (see Fig. 4, right). We assume a regime of small magnetic field (<1 mT) for which the electronic Zeeman interaction is much lower than the zero field energy splittings (at least a few 100s of MHz). In this case, the magnetic field effect on the ZEFOZ level energies can be calculated using second-order perturbation theory. Nuclear Zeeman interactions, which also appear at second order, are neglected.

For the excited state ZEFOZ levels, it is enough to consider only magnetic noise parallel to c as $g_\parallel \gg g_\perp$. Using the values

given in Table II for the hyperfine and Zeeman interactions, this leads to

$$E_{1,2}^0 = (A_\parallel \pm A_{\perp,1} \mp A_{\perp,2})/4, \tag{A1}$$

$$E_{3,4}^0 = (-A_\parallel \pm A_{\perp,1} \pm A_{\perp,2})/4, \tag{A2}$$

$$E_{1,2} = E_{1,2}^0 \pm \frac{\mu_B^2 g_\parallel^2 \delta B_\parallel^2}{2(A_{\perp,1} - A_{\perp,2})}, \tag{A3}$$

$$E_{3,4} = E_{3,4}^0 \pm \frac{\mu_B^2 g_\parallel^2 \delta B_\parallel^2}{2(A_{\perp,1} + A_{\perp,2})}. \tag{A4}$$

It can be noted that the matrix elements of the parallel Zeeman interaction are nonzero only between levels 1–2 and 3–4.

In the ground state, we considered only the ZEFOZ levels, labeled 3 and 4. In this case, the noise generated by fields perpendicular to c have to be considered too, resulting in

$$E_{1,2}^0 = A_\parallel/4, \tag{A5}$$

$$E_{3,4}^0 = (-A_\parallel \pm 2A_\perp)/4, \tag{A6}$$

$$E_3 = E_3^0 + \frac{\mu_B^2 g_\parallel^2 \delta B_\parallel^2}{4A_\perp} - \frac{\mu_B^2 g_\perp^2 \delta B_\perp^2}{2(A_\parallel - A_\perp)}, \tag{A7}$$

$$E_4 = E_4^0 - \frac{\mu_B^2 g_\parallel^2 \delta B_\parallel^2}{4A_\perp} - \frac{\mu_B^2 g_\perp^2 \delta B_\perp^2}{2(A_\perp + A_\parallel)}. \tag{A8}$$

From these expressions, the energies of the optical ZEFOZ transitions between the four excited-state levels and two ground-state levels were calculated and an average second-order sensitivity to magnetic noise determined. The average was carried out over all possible transitions, although a more accurate calculation should consider possible selection rules as a function of light polarization [18,58].

[1] C. Thiel, T. Böttger, and R. Cone, Rare-earth-doped materials for applications in quantum information storage and signal processing, J. Lumin. **131**, 353 (2011).

[2] P. Goldner, A. Ferrier, and O. Guillot-Noël, *Rare Earth-Doped Crystals for Quantum Information Processing* (Elsevier, Amsterdam, 2015), Chap. 267, pp. 1–78.

[3] D. D. Awschalom, R. Hanson, J. Wrachtrup, and B. B. Zhou, Quantum technologies with optically interfaced solid-state spins, Nat. Photonics **12**, 516 (2018).

[4] M. Afzelius and H. de Riedmatten, *Quantum Light Storage in Solid State Atomic Ensembles* (Springer, Cham, 2015).

[5] X. Fernandez-Gonzalvo, S. P. Horvath, Y.-H. Chen, and J. J. Longdell, Cavity-enhanced raman heterodyne spectroscopy in Er^{3+}:Y_2SiO_5 for microwave to optical signal conversion, Phys. Rev. A **100**, 033807 (2019).

[6] A. Kinos, D. Hunger, R. Kolesov, K. Mølmer, H. de Riedmatten, P. Goldner, A. Tallaire, L. Morvan, P. Berger, S. Welinski, K. Karrai, L. Rippe, S. Kröll, and A. Walther, Roadmap for Rare-earth Quantum Computing, arXiv:2103.15743.

[7] T. Böttger, C. W. Thiel, Y. Sun, and R. L. Cone, Optical decoherence and spectral diffusion at 1.5 μm in Er^{3+}:Y_2SiO_5 versus magnetic field, temperature, and Er^{3+} concentration, Phys. Rev. B **73**, 075101 (2006).

[8] T. Böttger, C. W. Thiel, R. L. Cone, and Y. Sun, Effects of magnetic field orientation on optical decoherence in Er^{3+}:Y_2SiO_5, Phys. Rev. B **79**, 115104 (2009).

[9] M. Rančić, M. P. Hedges, R. L. Ahlefeldt, and M. J. Sellars, Coherence time of over a second in a telecom-compatible quantum memory storage material, Nat. Phys. **14**, 50 (2018).

[10] J. J. Longdell, A. L. Alexander, and M. J. Sellars, Characterization of the hyperfine interaction in europium-doped yttrium orthosilicate and europium chloride hexahydrate, Phys. Rev. B **74**, 195101 (2006).

[11] M. Zhong, M. P. Hedges, R. L. Ahlefeldt, J. G. Bartholomew, S. E. Beavan, S. M. Wittig, J. J. Longdell, and M. J. Sellars, Optically addressable nuclear spins in a solid with a six-hour coherence time, Nature (London) **517**, 177 (2015).

[12] E. Fraval, M. J. Sellars, and J. J. Longdell, Method of Extending Hyperfine Coherence Times in Pr^{3+}:Y_2SiO_5, Phys. Rev. Lett. **92**, 077601 (2004).

[13] M. Lovrić, P. Glasenapp, D. Suter, B. Tumino, A. Ferrier, P. Goldner, M. Sabooni, L. Rippe, and S. Kröll, Hyperfine characterization and spin coherence lifetime extension in Pr^{3+}:$La_2(WO_4)_3$, Phys. Rev. B **84**, 104417 (2011).

[14] A. Ortu, A. Tiranov, S. Welinski, F. Fröwis, N. Gisin, A. Ferrier, P. Goldner, and M. Afzelius, Simultaneous coherence enhancement of optical and microwave transitions in solid-state electronic spins, Nat. Mater. **17**, 671 (2018).

[15] S. Welinski, A. Tiranov, M. Businger, A. Ferrier, M. Afzelius, and P. Goldner, Coherence Time Extension by Large-Scale Optical Spin Polarization in a Rare-Earth Doped Crystal, Phys. Rev. X **10**, 031060 (2020).

[16] M. Businger, A. Tiranov, K. T. Kaczmarek, S. Welinski, Z. Zhang, A. Ferrier, P. Goldner, and M. Afzelius, Optical Spin-Wave Storage in a Solid-State Hybridized Electron-Nuclear Spin Ensemble, Phys. Rev. Lett. **124**, 053606 (2020).

[17] J. V. Rakonjac, Y.-H. Chen, S. P. Horvath, and J. J. Longdell, Long spin coherence times in the ground state and in an optically excited state of $^{167}Er^{3+}$:Y_2SiO_5 at zero magnetic field, Phys. Rev. B **101**, 184430 (2020).

[18] J. M. Kindem, J. G. Bartholomew, P. J. T. Woodburn, T. Zhong, I. Craiciu, R. L. Cone, C. W. Thiel, and A. Faraon, Characterization of $^{171}Yb^{3+}$: YVO_4 for photonic quantum technologies, Phys. Rev. B **98**, 024404 (2018).

[19] J. G. Bartholomew, J. Rochman, T. Xie, J. M. Kindem, A. Ruskuc, I. Craiciu, M. Lei, and A. Faraon, On-chip coherent microwave-to-optical transduction mediated by ytterbium in YVO_4, Nat. Commun. **11**, 3266 (2020).

[20] J. M. Kindem, A. Ruskuc, J. G. Bartholomew, J. Rochman, Y. Q. Huan, and A. Faraon, Control and single-shot readout of an ion embedded in a nanophotonic cavity, Nature (London) **580**, 201 (2020).

[21] J. D. Witmer, J. A. Valery, P. Arrangoiz-Arriola, C. J. Sarabalis, J. T. Hill, and A. H. Safavi-Naeini, High-q photonic resonators

and electro-optic coupling using silicon-on-lithium-niobate, Sci. Rep. **7**, 46313 (2017).

[22] S. Chen, M. Raha, C. M. Phenicie, S. Ourari, and J. D. Thompson, Parallel single-shot measurement and coherent control of solid-state spins below the diffraction limit, Science **370**, 592 (2020).

[23] B. Casabone, C. Deshmukh, S. Liu, D. Serrano, A. Ferrier, T. Hümmer, P. Goldner, D. Hunger, and H. de Riedmatten, Dynamic control of purcell enhanced emission of erbium ions in nanoparticles, Nat. Commun. **12**, 3570 (2021).

[24] S. Marzban, J. G. Bartholomew, S. Madden, K. Vu, and M. J. Sellars, Observation of Photon Echoes from Evanescently Coupled Rare-Earth Ions in a Planar Waveguide, Phys. Rev. Lett. **115**, 013601 (2015).

[25] K. Xia, F. Sardi, C. Sauerzapf, T. Kornher, H.-W. Becker, Z. Kis, L. Kovacs, D. Dertli, J. Foglszinger, R. Kolesov, and J. Wrachtrup, Tunable microcavities coupled to rare-earth quantum emitters, Optica **9**, 445 (2022).

[26] A. Boes, B. Corcoran, L. Chang, J. Bowers, and A. Mitchell, Status and potential of lithium niobate on insulator (LNOI) for photonic integrated circuits, Laser Photonics Rev. **12**, 1700256 (2018).

[27] Y. Zheng and X. Chen, Nonlinear wave mixing in lithium niobate thin film, Adv. Phys.-X **6**, 1889402 (2021).

[28] C. Wang, M. Zhang, X. Chen, M. Bertrand, A. Shams-Ansari, S. Chandrasekhar, P. Winzer, and M. Lončar, Integrated lithium niobate electro-optic modulators operating at CMOS-compatible voltages, Nature (London) **562**, 101 (2018).

[29] J.-H. Kim, S. Aghaeimeibodi, J. Carolan, D. Englund, and E. Waks, Hybrid integration methods for on-chip quantum photonics, Optica **7**, 291 (2020).

[30] S. Dutta, E. A. Goldschmidt, S. Barik, U. Saha, and E. Waks, Integrated photonic platform for rare-earth ions in thin film lithium niobate, Nano Lett. **20**, 741 (2020).

[31] D. Pak, H. An, A. Nandi, X. Jiang, Y. Xuan, and M. Hosseini, Ytterbium-implanted photonic resonators based on thin film lithium niobate, J. Appl. Phys. **128**, 084302 (2020).

[32] N. Sinclair, D. Oblak, C. W. Thiel, R. L. Cone, and W. Tittel, Properties of a Rare-Earth-Ion-Doped Waveguide at Sub-Kelvin Temperatures for Quantum Signal Processing, Phys. Rev. Lett. **118**, 100504 (2017).

[33] P. Zarkeshian, C. Deshmukh, N. Sinclair, S. Goyal, G. Aguilar, P. Lefebvre, M. G. Puigibert, V. Verma, F. Marsili, M. Shaw *et al.*, Entanglement between more than two hundred macroscopic atomic ensembles in a solid, Nat. Commun. **8**, 906 (2017).

[34] S. Wang, L. Yang, R. Cheng, Y. Xu, M. Shen, R. L. Cone, C. W. Thiel, and H. X. Tang, Incorporation of erbium ions into thin-film lithium niobate integrated photonics, Appl. Phys. Lett. **116**, 151103 (2020).

[35] C. Thiel, R. Macfarlane, T. Böttger, Y. Sun, R. Cone, and W. Babbitt, Optical decoherence and persistent spectral hole burning in Er^{3+}: LiNbO$_3$, J. Lumin. **130**, 1603 (2010).

[36] C. Thiel, Y. Sun, R. Macfarlane, T. Böttger, and R. Cone, Rare-earth-doped LiNbO$_3$ and KTiOPO$_4$ (KTP) for waveguide quantum memories, J. Phys. B: At., Mol. Opt. Phys. **45**, 124013 (2012).

[37] Z. Kis, G. Mandula, K. Lengyel, I. Hajdara, L. Kovacs, and M. Imlau, Homogeneous linewidth measurements of Yb^{3+} ions in congruent and stoichiometric lithium niobate crystals, Opt. Mater. (Amsterdam) **37**, 845 (2014).

[38] T. Nolte, T. Pawlik, and J.-M. Spaeth, Epr study of Er^{3+} in congruent LiNbO$_3$, Solid State Commun. **104**, 535 (1997).

[39] Y. Sun, C. W. Thiel, and R. L. Cone, Optical decoherence and energy level structure of 0.1% Tm^{3+}:LiNbO$_3$, Phys. Rev. B **85**, 165106 (2012).

[40] G. Malovichko, V. Grachev, S. Okulov, E. Kokanyan, F. Henecker, A. Hofstaetter, and O. Schirmer, EPR of Nd^{3+} in congruent and nearly stoichiometric lithium niobate, Phys. Status Solidi B **243**, 409 (2006).

[41] G. Malovichko, V. Bratus1, V. Grachev, and E. Kokanyan, Electron paramagnetic resonance and electron-nuclear double resonance of nonequivalent Yb^{3+} centers in stoichiometric lithium niobate, Phys. Status Solidi B **246**, 215 (2009).

[42] T. Renner, *Quantities, Units and Symbols in Physical Chemistry* (Royal Society of Chemistry, Cambridge, UK, 2007), pp. 113–121.

[43] A. M. Stoneham, Shapes of inhomogeneously broadened resonance lines in solids, Rev. Mod. Phys. **41**, 82 (1969).

[44] F. Könz, Y. Sun, C. W. Thiel, R. L. Cone, R. Equall, R. Hutcheson, and R. M. Macfarlane, Temperature and concentration dependence of optical dephasing, spectral-hole lifetime, and anisotropic absorption in Eu^{3+}:Y$_2$SiO$_5$, Phys. Rev. B **68**, 085109 (2003).

[45] T. Böttger, C. W. Thiel, R. L. Cone, Y. Sun, and A. Faraon, Optical spectroscopy and decoherence studies of Yb^{3+}:YAG at 968 nm, Phys. Rev. B **94**, 045134 (2016).

[46] R. M. Macfarlane, F. Könz, Y. Sun, and R. L. Cone, Spectral hole burning and optical dephasing in disordered crystals—Pr^{3+}: LiNbO$_3$ and Pr^{3+}:Sr$_{.6}$Ba$_{.4}$Nb$_2$O$_6$ (SBN), J. Lumin. **86**, 311 (2000).

[47] H. G. Demirkhanyan, G. G. Demirkhanyan, V. G. Babajanyan, R. B. Kostanyan, and E. P. Kokanyan, Spectral line intensities of Yb^{3+} ion in LiNbO$_3$ crystals, J. Contemp. Phys. (Arm. Acad. Sci.) **43**, 13 (2008).

[48] G. Liu and B. Jacquier, *Spectroscopic Properties of Rare Earths in Optical Materials* (Springer Science & Business Media, Berlin, 2006), Vol. 83.

[49] U. Schlarb and K. Betzler, Refractive indices of lithium niobate as a function of temperature, wavelength, and composition: A generalized fit, Phys. Rev. B **48**, 15613 (1993).

[50] D. L. McAuslan, J. J. Longdell, and M. J. Sellars, Strong-coupling cavity QED using rare-earth-metal-ion dopants in monolithic resonators: What you can do with a weak oscillator, Phys. Rev. A **80**, 062307 (2009).

[51] E. Montoya, F. Agullo-Rueda, S. Manotas, J. G. Solé, and L. Bausá, Electron–phonon coupling in Yb^{3+}: LiNbO$_3$ laser crystal, J. Lumin. **94–95**, 701 (2001).

[52] A. Tiranov, A. Ortu, S. Welinski, A. Ferrier, P. Goldner, N. Gisin, and M. Afzelius, Spectroscopic study of hyperfine properties in $^{171}Yb^{3+}$:Y$_2$SiO$_5$, Phys. Rev. B **98**, 195110 (2018).

[53] R. Orbach and H. J. Stapleton, *Electron Spin-Lattice Relaxation* (Plenum, New York, 1972).

[54] P. Hu and L. R. Walker, Spectral-diffusion decay in echo experiments, Phys. Rev. B **18**, 1300 (1978).

[55] D. L. Huber, M. M. Broer, and B. Golding, Low-Temperature Optical Dephasing of Rare-Earth Ions in Glass, Phys. Rev. Lett. **52**, 2281 (1984).

[56] Y. C. Sun, *Rare Earth Materials in Optical Storage and Data Processing Applications* (Springer, Berlin, 2005), pp. 379–429.

[57] W. B. Mims, Phase memory in electron spin echoes, lattice relaxation effects in $CaWO_4$: Er, Ce, Mn, Phys. Rev. **168**, 370 (1968).

[58] M. Afzelius, M. U. Staudt, H. de Riedmatten, N. Gisin, O. Guillot-Noël, P. Goldner, R. Marino, P. Porcher, E. Cavalli, and M. Bettinelli, Efficient optical pumping of Zeeman spin levels in Nd^{3+}: YVO4, J. Lumin. **130**, 1566 (2010).